

1 **Mapping and evaluating kinematics and stress/strain field at active**  
2 **faults and fissures: a comparison between field and drone data at NE**  
3 **Rift, Mt Etna (Italy)**

4  
5 Alessandro Tibaldi<sup>1,2\*</sup>, Noemi Corti<sup>1</sup>, Emanuela De Beni<sup>3</sup>, Fabio Luca Bonali<sup>1,2</sup>, Susanna Falsaperla<sup>3</sup>,  
6 Horst Langer<sup>3</sup>, Marco Neri<sup>3</sup>, Massimo Cantarero<sup>3</sup>, Danilo Reitano<sup>3</sup>, Luca Fallati<sup>1</sup>  
7

8 <sup>1</sup> Department of Earth and Environmental Sciences, University of Milan-Bicocca, Milan, Italy  
9 <sup>2</sup> CRUST- Interuniversity Center for 3D Seismotectonics with Territorial Applications, Italy  
10 <sup>3</sup> Istituto Nazionale di Geofisica e Vulcanologia, Osservatorio Etneo, Sezione di Catania, Italy  
11

12 \* Corresponding author: [alessandro.tibaldi@unimib.it](mailto:alessandro.tibaldi@unimib.it), Tel.: +390264482032  
13  
14

15 **Abstract**

16 We collected drone data to quantify the kinematics at extensional fractures and normal faults,  
17 integrated this information with seismological data to reconstruct the stress field, and critically  
18 compared the results with previous fieldwork to assess the best practice. As key site, we analysed a  
19 sector of the North-East Rift of Mt Etna, an area affected by continuous ground deformation linked  
20 to gravity sliding of the volcano's eastern flank and dyke injections. The studied sector is  
21 characterized also by the existence of eruptive craters and fissures and lava flows. This work shows  
22 that this rift segment is affected by a series of NNE- to NE-striking, parallel extensional fractures  
23 characterized by an opening mode along an average N105.7° vector. The stress field is characterised  
24 by a  $\sigma_{Hmin}$  trending NW-SE. Normal faults strike parallel to the extensional fractures. The extensional  
25 strain obtained by cumulating the net offset at extensional fractures with the fault heave gives a  
26 stretching ratio of 1.003 in the northeastern part of the study area and 1.005 in the southwestern  
27 part. Given a maximum age of 1614 yr AD for the offset lavas, we obtained an extension rate of 1.9  
28 cm/yr for the last 406 yr. This value is consistent with the slip along the Pernicana Fault System,  
29 confirming that they accommodate the sliding of the eastern flank of the volcano.  
30

31 **Keywords:** Drone; Structure from Motion; rift; Etna; normal faults  
32  
33  
34

35 **1. Introduction**

**Spostato (inserimento) [1]**

**Eliminato:** , although they tend to bend slightly when crossing topographic highs corresponding to pyroclastic cones

**Spostato in su [1]:** The stress field is characterised by a  $\sigma_{Hmin}$  trending NW-SE.

**Eliminato:** Results indicate that Structure-from-Motion photogrammetry applied to drone surveys allows to collect large amounts of data with a resolution of 2-3 cm, a detail comparable to field surveys. In the same amount of time, drone survey can allow to collect more data than classical fieldwork, especially in logistically difficult rough terrains.

**Eliminato:** ¶

47 Quantifying offset at recent and active faults and other structures is fundamental to decipher the  
48 kinematics and stress/strain of deformation zones. This is a basic step for the assessment of seismic  
49 hazard (Lyakhovsky et al., 2012); it also contributes in the case of volcanic zones to the  
50 understanding of the crustal conditions that may facilitate magma ascent and thus the evaluation  
51 of volcanic hazard (Keir et al., 2006). At rift zones, the precise definition of the spreading direction  
52 and extensional rate requires the collection of a huge amount of data that must cover the whole rift  
53 extension. Since rift zones are composed of swarms of tens to hundreds normal faults and extension  
54 fractures, the collection of a statistically robust amount of data requires a heavy effort of fieldwork.  
55 Moreover, logistically complex conditions can affect the performance of fieldwork, as for example  
56 in the Eastern Africa rift system, where crustal extension rates have been frequently evaluated  
57 indirectly from plate tectonic models (Jestin et al., 1994; Chu and Gordon, 1999).  
58 On active volcanoes, the presence of rough terrains and the possible exposition of researchers to  
59 explosive products frequently prevent optimal field surveys. These complex logistic conditions, in  
60 fact, do not permit to have a detailed evaluation of the strain field due to the difficulties to obtain  
61 a sufficiently large number of measurements along an extension fracture or a fault. In fact, only the  
62 collection of a large amount of horizontal dilation values can allow the precise reconstruction of the  
63 strain field. At faults, the reconstruction of heave and throw values requires the precise  
64 measurement of offset. Anyway, the measurement of fault slip profiles is very time-consuming and  
65 can be very difficult in the case of faults with offsets in the order of tens of meters.

Eliminato: huge

66 In the last few years, the above-mentioned difficulties have been overcome by the use of Structure-  
67 from-Motion (SfM) photogrammetry applied to images collected by Unmanned Aerial Vehicles  
68 (UAVs or drones), in active volcano-tectonics studies (Bonali et al., 2019a, 2020; Trippanera et al.,  
69 2019; Weismüller et al., 2019) and to assess volcanic hazard (Müller et al., 2017; Darmawan et al.,  
70 2018; De Beni et al., 2019). Therefore, in this work we use this technique, which allows us to  
71 reconstruct very detailed Orthomosaics and Digital Surface Models (DSMs) of the surveyed areas.  
72 The resulting images, which can attain a resolution as precise as 1 cm, allow to collect several high-  
73 resolution structural data also in 3D, and take direct measurements of structures and  
74 morphostructures, like dilation values along faults and fractures, even using immersive Virtual  
75 Reality tools (Tibaldi et al., 2020).

Eliminato: T

Eliminato: ,

76 The present paper has a double focus: on one side it describes new data useful for the interpretation  
77 of the activity of the NE Rift, and on the other side it aims to present a methodology useful for  
78 similar studies. We show that the UAV-supported methodology can attain a precision comparable

Eliminato: in t

Eliminato: ,

Eliminato: w

85 to field surveys in areas affected by active deformation. We also wish to show that UAV surveys  
86 have a sufficient precision that may allow to quantify the increment of extensional deformation by  
87 successive, repeated surveys. For this, we selected a sector of the NE Rift, located on the northern  
88 summit part of Mt Etna (Italy) (Fig. 1), which is characterized by ongoing extensional fracturing,  
89 eruptive fissuring and normal faulting. This also contributes to improve our knowledge of this  
90 important volcanotectonic structure of Mt. Etna, where only a few structural surveys were  
91 conducted several years ago by Garduño et al. (1997) and Tibaldi and Groppelli (2002). The 2002-  
92 2003 eruption took place here accompanied by the development of new fractures and deposits, and  
93 thus a new mapping is necessary.

94 The area turned out to be very suitable for such studies because: i) it is not covered by vegetation  
95 due to the high altitude (2000-2500 m a.s.l.); ii) it is characterized by high deformation rates (in the  
96 order of 2 cm/yr, Tibaldi and Groppelli, 2002); iii) the deposits affected by faulting and fracturing  
97 are historic, and as a consequence the effects of erosion are negligible and structures are perfectly  
98 preserved.

99

## 100 2. Geological background

101 Mt Etna, one of the most active volcanoes on Earth, is located in a compressional environment  
102 (Lanzafame et al., 1997; Cocina et al., 1997, 1998), at the border between the African and the  
103 European Plate (Fig. 1A).

104 Etna volcano has a constantly opened central conduit feeding four summit craters named Voragine  
105 (VOR; formed in 1945), Northeast Crater (NEC; 1911), Bocca Nuova (BN; 1968) and Southeast Crater  
106 (SEC; 1971) (Fig. 1C). After 2007, a new large summit cone grew on the southeast flank of the SEC:

107 the New South-East Crater (Del Negro et al., 2013; Behncke et al., 2014; Acocella et al., 2016).

108 Eruptions from these summit craters are classified as summit eruptions (Acocella and Neri, 2003).

109 Flank eruptions occur along radial fissures mostly on three main "rift zones": the W Rift, the S Rift  
110 and the NE Rift (Fig. 1B) (Cappello et al., 2012). These flank (or lateral) eruptions are usually fed by  
111 shallow (1-3 km) dykes that propagate laterally from the central conduit (Acocella and Neri, 2009).

112

**Eliminato:** it is possible to collect data in an active rift with a so high precision that future UAV surveys in the same area could allow the collection of sufficient data to resolve the increment of extensional deformation.

**Eliminato:** its current activity is characterized by central eruptions from four summit craters and flank eruptions along different rift zones, such as the NE Rift (Fig. 1B) (Cappello et al., 2012), associated with a diffuse volcano-tectonic seismicity.

**Eliminato:** huge

**Eliminato:** ows

**Eliminato:** one of

**Eliminato:** focused

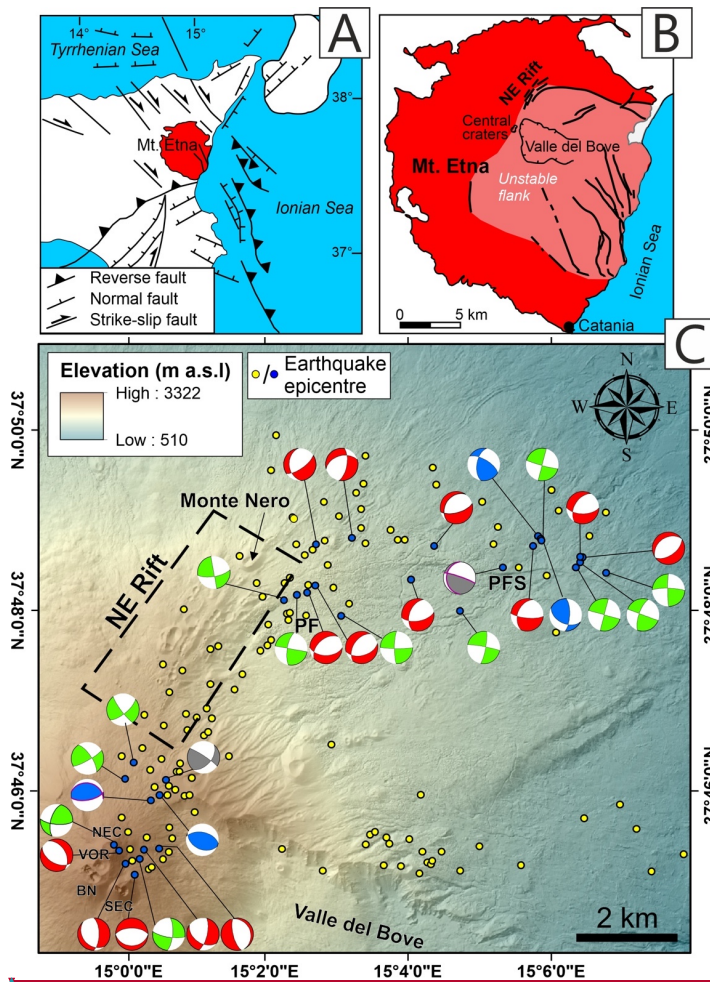
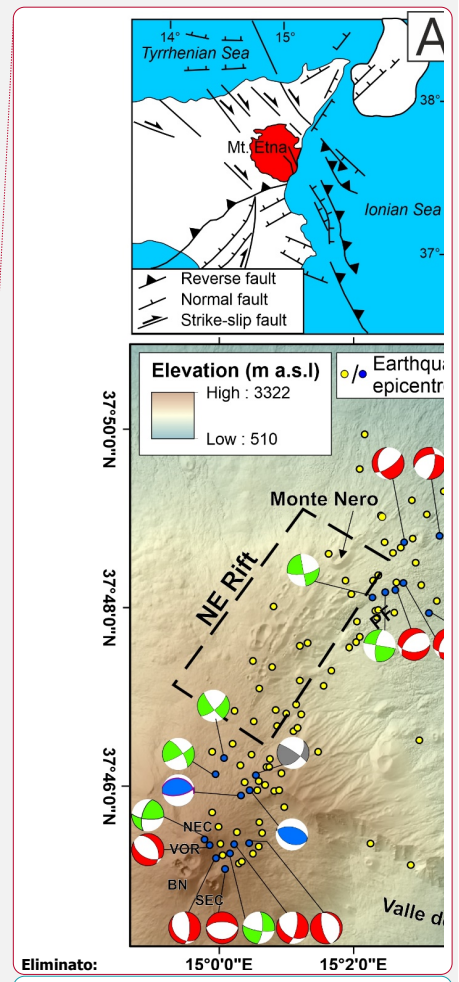


**Figure 1.** (A) Map showing the geodynamic context where Etna Volcano locates; (B) Map showing the main structures of Mt Etna, with the eastern flank characterized by instability (A and B modified after Villani et al., 2020). (C) Digital Elevation Model of the upper part of Mt Etna with location of the 118 well-constrained earthquake epicenters (yellow dots) occurred during the 2002-2003 eruption (data credits: Tiziana Tuvè, INGV), and available focal mechanisms between 2008 and 2019 (blue dots) (source: [http://sismoweb.ct.ingv.it/maps/eq\\_maps/focals/index.php](http://sismoweb.ct.ingv.it/maps/eq_maps/focals/index.php)). The location errors of the data set are on average 0.62 km for the epicenter and 0.41 km for the depth. Corresponding values for the median are 0.3 km (epicenter) and 0.1 km (depth). For more details on the location uncertainties, see Figs. 4 and 5 of Mostaccio et al. (2013). The black rectangle locates the area of NE Rift represented in Figures 2 and 3. PF: Piano Provenzana Fault, PFS: Pernicana Fault System, NEC: North-East Crater, VOR: Voragine Crater, BN: Bocca Nuova Crater, SEC: South-East Crater.



Eliminato:  
Formattato: Colore carattere: Testo 1  
Eliminato: location of Mt. Etna

Codice campo modificato

140

141 The NE Rift is a network of N- to NE-striking eruptive fissures, 0.5 km wide and about 7 km long,  
142 extending from the NEC (~3320 m a.s.l.) to ~1400 m of altitude (Garduño et al., 1997) (Fig. 2). The  
143 upper portion of the rift strikes N from the summit down to 2500 m a.s.l., whereas the lower section  
144 strikes NE down to the Monte Nero area (Fig. 1C). The rift is bordered to the southeast by a 200-m-  
145 high tectonic scarp (Piano Provenzana fault, PF in Figs. 1C and 2) partially covered by recent volcanic  
146 products. To the west, the rift is limited by a small scarp, crossed by recent eruptive fissures and  
147 largely concealed by historic lava flows and cinder cones. Faults and non-eruptive fractures cut the  
148 central portion of the NE Rift; they strike between 0° and 60° and have different kinematics,  
149 including pure extension or right-lateral and left-lateral transtension (Tibaldi and Groppelli, 2002).  
150 About 35% of the fractures are associated with extrusive volcanic activity, which affected the lower  
151 portion of the same fractures: along these, hornitos, craters, small and large cinder cones are  
152 common. Moving downslope, cones and craters take on more and more a pronounced elliptical  
153 shape, with the main axis striking 30°-60°. Within them, the feeding magmatic dyke often crops out,  
154 striking 10-20° in the central part of the rift, and 40-50° in the northeastern part (Geshi and Neri,  
155 2014).  
156 At ~1800 m a.s.l., the NE Rift meets the 18-km-long Pernicana Fault System (PFS, Figs. 1C and 2), an  
157 active left-lateral transtensional structure bounding the unstable flank of the volcano (Groppelli and  
158 Tibaldi, 1999; Acocella and Neri, 2005). Both the NE Rift and the PFS are the NW margins of a wide  
159 sector of Etna involved in seaward displacement (Fig. 1B) (Borgia et al., 1992; Solaro et al., 2010;  
160 Ruch et al., 2010, 2013; Acocella et al., 2013; Apuani et al., 2013; Mattia et al., 2015), affecting an  
161 onshore area >700 km<sup>2</sup> (Neri et al., 2004) and with a thickness of 1-4 km (Ruch et al., 2010;  
162 Siniscalchi et al., 2012; Ruch et al., 2012). This corresponds to the unstable flank delimited by the  
163 upper slip surface of Guardo et al. (2020), since this upper surface tends to emerge in  
164 correspondence of the Etna summit – NE Rift zone, and goes from above sea level down to almost  
165 4 km b.s.l., from west to east. The unstable area also continues below sea level, until it reaches the  
166 abyssal plain at a depth of over 2000 meters (Urulaub et al., 2018). Several authors have recently  
167 highlighted the possible relationship between eruptive activity and flank deformation, showing that  
168 the acceleration of flank deformation may trigger flank eruptions and vice versa. In some cases, it  
169 was demonstrated that tectonic activity along the PFS triggers eruptions from the NE Rift (Neri et  
170 al., 2004, 2005; Walter et al., 2005; Bonforte et al., 2011; Ruch et al., 2012; De Novellis et al., 2019).

Eliminato: dry

Eliminato: , part of which indicating

Eliminato: both

Eliminato: (middle portion

Eliminato: )

Eliminato: lower portion;

Eliminato: Actually

Eliminato: ,

Formattato: Non Evidenziato

Formattato: Non Evidenziato

Eliminato: .

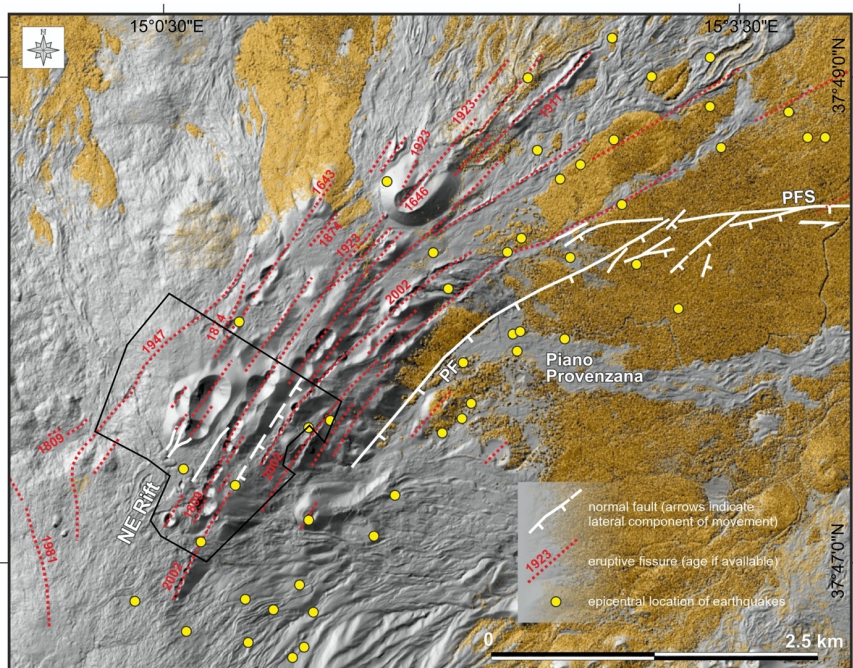
180 Applying the lithostratigraphic units following the standards suggested by Salvador (1994), two main  
181 groups of volcanic deposits are detectable in the NE Rift area (Fig. 3): the products belonging to the  
182 Il Piano Synthem (Mongibello Volcano Lithosomatic Unit; 15,420±60 - 0 a BP) and those belonging  
183 to the Concazze Synthem (Ellittico volcano Lithosomatic Unit; 56.6±15.4 ka - 15,420±60 a BP)  
184 (Coltelli et al., 1994; Garduño et al., 1997; Coltelli et al., 2000). Both represent volcanic units made  
185 up of products erupted during the last ~57 ka and belonging to the Mongibello Supersynthem  
186 (Branca et al., 2011).

187 With reference to the stratigraphy in the bottom part of Figure 3, the Concazze Synthem coincides  
188 with Ellittico Volcano, a large stratovolcano with a main, summit eruptive vent approximately  
189 coinciding with the current summit of Etna, but higher (3600-3800 m a.s.l.). The stratigraphic  
190 succession consists of alternating lavas and pyroclastic deposits. It ends with plagioclase-rich  
191 porphyritic lava flows and reddish subaphiric lavas and scorias (Pizzi Deneri Formation and Portella  
192 Giumenta formation, respectively; Coltelli et al., 1994; Branca et al., 2011). The deposits of the final  
193 explosive activity at Ellittico date at 15,420±60 a BP (Condomines et al., 1982; Cortesi et al., 1988;  
194 Gillot et al., 1994; Coltelli et al., 2000; De Beni et al., 2011); this explosive activity also generated the  
195 formation of a large and deep summit caldera, whose remains today crop out at the edge of the  
196 highest portion of the NE rift, namely at Punta Lucia and Pizzi Deneri. In the NE-Rift area, the  
197 products of Portella Giumenta formation overlap deeply eroded cinder cones and porphyritic lavas  
198 belonging to Piano Provenzana formation.

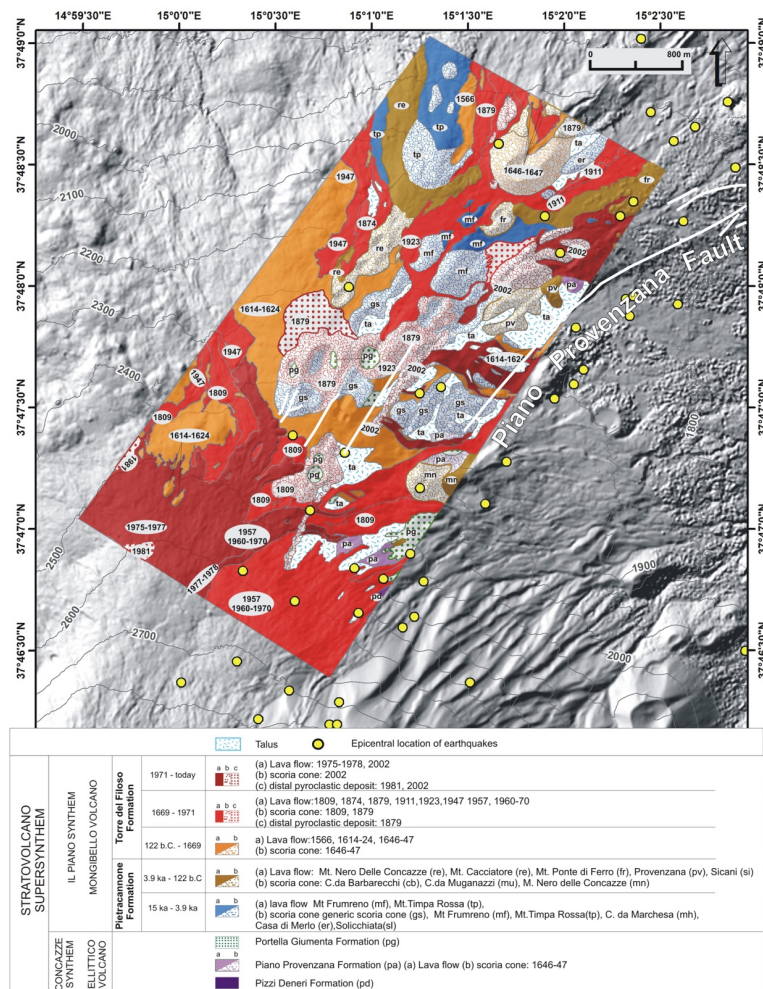
199 The Il Piano Synthem constitutes the present active volcano. The lower boundary coincides with the  
200 Ellittico caldera, while the upper boundary is the current topographic surface. In the NE Rift, the  
201 volcanics belonging to the Pietracannone and Torre del Filosofo formations largely crop out. During  
202 the last 120 years, the NE Rift eruptions lasted 21 days on average, with  $7 \text{ m}^3\text{s}^{-1}$  eruption rates. The  
203 eruptive fissures reached in ~1 day the maximum length (3825 m) by propagating at an average  
204 speed of  $0.053 \text{ ms}^{-1}$  (Neri et al., 2011).

205  
206  
207





208  
 209 **Figure 2.** Structural map of the NE Rift superimposed on a shaded relief Lidar derived image of the  
 210 area. Numbers show date of historical eruptive fissures (dotted red lines), modified after Neri et al.  
 211 (2004). Yellow circles mark the epicentral location of earthquakes recorded during the 2002-2003  
 212 eruption (for location error see caption of Fig. 1). In white major faults, PF: Piano Provenzana Fault,  
 213 PFS: Pernicana Fault System. The area outlined by the black line represents the area of Figures 5-6  
 214 surveyed with the drones. The NE Rift is located in Figure 1.



215

216 **Figure 3.** Geological map of the NE Rift showing lithostratigraphic units, the 2002-2003 earthquake  
217 epicenters (yellow dots), and the main faults (in white), superimposed on a shaded relief DSM derived  
218 of the area (Gwinner et al., 2006). The NE Rift is located in Figure 1.

219

### 220 3. Seismological data

221 Number of stations and geometry of the seismic network for the permanent monitoring of Etna  
222 significantly changed in the last 40 years. The boost of the seismic network (from five short period,  
223 vertical-component stations of the 1970s to the 30 broadband, 3-component sensors of 2020) has  
224 also involved signal transmission (from analogue to digital) and acquisition systems (Patanè et al.,



225 2004). In the framework of seismic activity at Etna, the NE rift, along with the PFS and the PF, plays  
 226 a key role. Indeed, they form a discontinuity that accommodates stress changes related to the  
 227 magma intrusion and tectonic loading, interpreted as the main sources causing the eastward sliding  
 228 of the eastern sector of the volcano (Alparone et al., 2013a,b).

229 The area of interest in this case study is situated at the westernmost part of the PFS-PF fault system.  
 230 The structure has a bow-like geometry, striking NE at its western tip, and bending along an E-W  
 231 strike direction towards east. Here the earthquakes are usually shallow (depths mostly between 0  
 232 and 3 km b.s.l.) and with small to moderate magnitude ( $M_L < 5$ ) (Fig. 1C). Despite their magnitude,  
 233 these superficial earthquakes can be damaging as documented by macroseismic studies, which  
 234 highlight the high seismic hazard of this sector of the volcano (Azzaro et al., 1998; Azzaro, 2004).  
 235 Alparone et al. (2013a,b) report that seismic activity at the PFS-PF fault system increased from  
 236 September 2002 on, starting shortly (a month) before the 2002-2003 eruption. Overall, 874  
 237 earthquakes with  $M_{max}$  4.1 heralded the onset of that eruptive episode. Focusing on seismic  
 238 activity during the 2002-2003 eruption, Mostaccio et al. (2013) tested NonLinLoc (Lomax et al.,  
 239 2000), a nonlinear probabilistic earthquake location method, using a 3D velocity model. From the  
 240 328 well-constrained locations obtained by Mostaccio et al. (2013), we extracted a subset of 118  
 241 shallow earthquakes, which are located in an area encompassing the zone of our case study, part of  
 242 the Valle del Bove and of the PFS-PF fault system. We used this 2002-2003 dataset because it  
 243 contains the best located earthquakes and because it is representative of the typical seismic activity  
 244 of this sector of Mt Etna. Figure 1C highlights a bow-shaped distribution of 90 epicentres starting  
 245 from the summit caters. The striking correlation between epicentre location and structural  
 246 elements is visible comparing Figure 1 and Figure 2, since both have an arcuate shape and seismicity  
 247 recalls the bow shape of the faults and fracture distribution. Along the NE Rift, the earthquake  
 248 distribution trends NNE-SSW, and tends to bend to NE-SW and E-W moving in eastern direction.  
 249 This group of earthquakes is well separated from a second, smaller group (26) located more to the  
 250 south, whose position clearly marks the northern rim of the Valle del Bove (Figure 1). It is worth  
 251 noting that the peculiar distribution of earthquakes in Figure 1 is not only typical of the 2002-2003  
 252 eruptive period. Indeed, analysing the distribution of seismic foci during the years from 2000 to  
 253 2009 (with the exclusion of time spans with volcanic activity), Alparone et al. (2013a,b) identified a  
 254 cluster of earthquakes, which closely marked the NE Rift and are aligned along the PFS-PF fault  
 255 system. The magnitude of these earthquakes was small, with only two of them with  $M_L > 2$ . A second

Eliminato: the

Eliminato: of which

Eliminato: here

Eliminato: M

cluster belonged to the easternmost sector of the PFS-PF; they had stronger magnitude, reaching values  $M_L$  4.1.

Figure 1C depicts the fault plane solution calculated for the earthquakes reported in Table S1 (attached file), which occurred from 2008 to 2019 (source: [http://sismoweb.ct.ingv.it/maps/eq\\_maps/focals/index.php](http://sismoweb.ct.ingv.it/maps/eq_maps/focals/index.php)). Even though the mechanisms show some scatter, common elements may be identified. The earthquakes located in the southwestern corner of the picture have T axes striking mostly N, NE and ENE. Most of these earthquakes have strike-slip or normal faulting mechanisms, with almost vertical P-axes. The earthquakes located in the northern part of the figure express the general trend of deformation along the PFS-PF fault system, with either normal faulting or horizontal strike-slip mechanism. All mechanisms of this group have T-axes striking in SE direction.

271

#### 272 4. Methods

##### 273 4.1 Drone survey, photo and GCPs collection

In the present work, we applied the Structure from Motion (SfM) photogrammetry techniques, through drone surveys, to build up the high-resolution Digital Surface Model (DSM) and Orthomosaic for the target area. We followed the overall workflow that has been successfully tested in volcanic terrains and in challenging logistic conditions (Bonali et al., 2019a, 2020). Such a workflow has been designed to work with commercial quadcopters over large areas in volcanic terrain, that is exactly the situation we tackled in the present work where we used the DJI Phantom 4 PRO. This device is supplied with an incorporated chipset to work with space-based satellite navigation/referencing system (GPS/GLONASS), and a high-resolution camera sensor (20 Megapixels) in order to enhance the quality of the surveying, as well as to obtain georeferenced pictures (Geographic coordinates/WGS84). The overall area has been surveyed by several different flight missions where each of them has been planned to consider the presence of natural obstacles - mainly identified as topographic highs - known from a previous field survey, topographic maps and satellite images. Flight height has been set up to 80-95 m above the ground, reaching the excellent pixel size of 2-3 cm for the resulting Orthomosaic. We set the flight path considering the wind speed and direction, and chose an overlap ratio of 85% and 80 %, along the flight path and in lateral direction, respectively (Gerloni et al., 2018; Antoniou et. al., 2019; Bonali et al., 2019a, 2020; Fallati et al., 2020). The constant speed velocity was set up by the app considering all above settings, and pictures have been captured using equal time interval modality.

**Eliminato:** The area has been consequently divided into 14 subareas, producing KML files to be managed in DJI Ground Station PRO app. The latter is the official app from DJI, working with IOS system, designed for drones mission planning and operating, available at: <https://www.dji.com/ground-station-pro>. Each flight mission has been set up in the app to work with one single battery, considering that the meteorological conditions at the altitude of 2300 m a.s.l., as well as the wind speed and direction, can change in a few minutes.

**Eliminato:**

As a parallel and complementary activity to the UAV survey, we collected several Ground Control Points (GCPs), distributed all over the area, essential to scale and reference the SfM-derived models, as well as to avoid any bulging effect (James and Robson, 2012; Turner et al., 2012; Westoby et al., 2012; Smith et al., 2016; Vollgger and Cruden, 2016; James et al., 2017; Esposito et al., 2017). We targeted 34 natural targets, as already successfully performed by Bonali et al. (2020), to speed up the GCPs collection avoiding the deployment and recovery of artificial targets. This method allowed us to save one day (8 hours) of fieldwork. All GCPs have been collected with the GPS/GNSS Stonex S850A multi-frequency receiver in RTK configuration (with sub-centimetre accuracy). Depending on the 3G network availability, the GPS was linked in real time with sicili@net network, a real-time correction service based on the caster NTRIP tool (<http://193.206.223.39:5099/spiderweb/frmIndex.aspx>) or, in base-rover configuration, data have been post-processed thanks to Stonex Cube manager using Monte Conca and Pizzi Deneri permanent station correction-data of the INGV network.

#### 4.2 Photogrammetry processing

For the photogrammetry processing of the 4018 captured pictures, we used a commercial SfM software - Agisoft METASHAPE (<http://www.agisoft.com/>), which is commonly used due to the outstanding quality of the resulting output models (Cook, 2017; Burns and Delparte, 2017; Benassi et al., 2017). We also used the Agisoft Cloud beta service for data processing. The processing passed through some key steps (workflow), described in detail by Verhoeven (2011) and Brunier et al. (2016), which led to the realization of the DSM and the Orthomosaic as final products (see Fig. 4 and Tables 1-2), that are based on the SfM-derived sparse and dense clouds.

We divided the overall workflow in four principal steps: i) aligning of pictures, ii) georeferencing, iii) Dense Cloud generation, and iv) DSM and Orthomosaic production. A summary of all details regarding the photogrammetry processing and results are reported in Table 1 and 2.

**Eliminato:** to save plenty of time.

**Formattato:** Colore carattere: Collegamento ipertestuale

**Codice campo modificato**

**Eliminato:** - characterized by an intuitive workflow, a user-friendly interface and a feasible educational license price; in addition, such software

**Eliminato:** also

**Eliminato:** Such a cloud service provides a virtual machine equipped as follow: CPU - 32 vCPU (2.7 GHz Intel Xeon E5 2686 v4), GPU 2 x NVIDIA Tesla M60, and RAM 240 GB. Thanks to the above points, the software is nowadays worldwide used by the Earth Science community.

**Eliminato:** ¶

**Eliminato:** A

**Eliminato:**

**Eliminato:** : pictures have been aligned using high accuracy settings, both reference and generic preselection, and 40,000 and 4000 as number values for Tie and Key points settings, respectively. ¶

**Eliminato:** G

**Eliminato:** : all GCPs were distinguished within the pictures, assigning the surveyed coordinates to the corresponding points/markers, allowing the scaling, and georeferencing, of the point clouds, thus improving the final model accuracy. ¶

**Eliminato:**

**Eliminato:** : we generated the 3-D dense point cloud from the sparse cloud, using the medium quality settings and the mild depth filtering. ¶

D

**Eliminato:** : in this step, the DSM was produced from the dense cloud, setting the projection to UTM33/WGS84. Afterwards, the Orthomosaic was generated using the DSM as reference and Mosaic (default) as blending mode

**Eliminato:** ¶

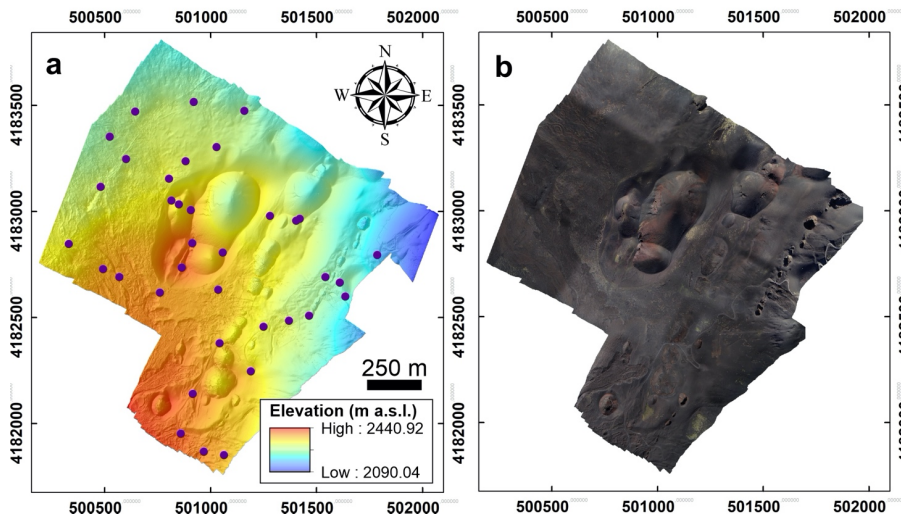


**Figure 4.** Resulting DSM (a) and Orthomosaic (b) of the surveyed area, blue dots represent the location of surveyed GCPs. Ref. system: UTM33/WGS84.

**Table 1.** Summary of setting and results related to the photogrammetry processing.

SfM Photogrammetry processing	Alignment processing settings	High accuracy / Generic and Reference Preselection
	Key Point / Tie Point limit	40,000 / 4,000
	Resulting Tie Points	1,773,948
	Dense Cloud processing settings	Medium Accuracy / Mild Filtering
	Resulting Dense Cloud (Points)	167,634,83
	Resulting DSM Resolution	11.86 cm/pix
	Resulting Orthomosaic	2.97 cm/pix

**Table 2.** Outline of time production for DSM and Orthomosaic, including the time (in hh:mm:ss) for UAV survey and image collection.

UAV survey / Images Acquisition	SfM Photogrammetry Processing time							Overall total
	Tie Points		Depth maps	Dense Cloud	DSM	Orthomosaic	Total for SfM	
	Matching	Alignment						
3:07:00	1:18:00	0:40:06	7:11:00	2:06:00	0:14:18	1:50:00	13:19:24	16:26:24

#### 4.3. Mapping and measurements gathering on SfM-derived models

The DSM and the Orthomosaic have been uploaded in a GIS environment, where we were able to trace all normal faults, extension fractures and eruptive fissures we recognized in the area (Fig. 5a).

Eliminato:

375 Structures with a continuous vertical offset > 20 cm, as measured on the DSM, have been classified  
376 as normal faults, whereas structures with vertical offset < 20 cm have been classified as extension  
377 fractures. Regarding eruptive fissures, they have been traced considering morphometric parameters  
378 of the eruptive centres, as explained in Tibaldi (1995), Bonali et al. (2011) and Tibaldi and Bonali  
379 (2017): the strike of the feeding fracture is directly related to the elongation of the cone base and  
380 the crater, to the direction of the line connecting the depressions on the crater rim, and to the  
381 alignment of cones. In some eruptive centres, the outcropping dyke was visible, giving information  
382 about the direction and component of opening of the eruptive fissure.

383 On the base of the derived models, we collected a total of 574 structural data (432 at extension  
384 fractures and 142 at faults); on the DSM, we measured strike and vertical offset along the normal  
385 faults, by calculating the difference in elevation along topographic profiles traced every 10 m,  
386 orthogonally to the fault scarp. With regard to extension fractures, we determined the local strike,  
387 the opening direction vector and the amount of net dilation. The latter two values were obtained  
388 by tracing a line that connects the two piercing points located on the opposite sides of an extension  
389 fracture, whenever they were undoubtedly recognizable. The length of the line gives the net dilation  
390 and related opening vector.  
391 Finally, along two NW-SE-trending transects traced parallel to the resulting overall direction of  
392 opening, the total amount of horizontal dilation has been calculated, cumulating each single value,  
393 as well as the extension rate and stretch in the area. These values were compared with the data  
394 collected in the field by Tibaldi and Groppelli (2002).

## 396 5. Results

397 We surveyed an area of 2.2 km<sup>2</sup> through the collection of a total of 4018 photos. Thanks to the  
398 above-described workflow, a high quality Orthomosaic and a DSM were reconstructed (Fig. 4), with  
399 a resulting ground resolution of 2.97 and 11.86 cm/pixel, respectively. On these models, we  
400 recognized the presence of 20 normal fault segments, 250 extension fractures and 54 eruptive  
401 fissures (Fig. 5a). The extension fractures strike mainly N20-50°, as highlighted in Figure 5b, with an  
402 average strike of N24.6°. Normal faults strike mainly N10-40° (Fig. 5c) with an average strike of  
403 N25.3°, whereas eruptive fissures strike mainly N20-40° (Fig. 5d) with an average strike of N29.8°.  
404 Regarding normal faults, they depict a graben running at the foothill of the westernmost pyroclastic  
405 cone, known as Monte Pizzillo (Fig. 5a). These faults have a maximum height of the SE-dipping scarp  
406 of 2.3 m (Fig. 6a), giving a heave of 0.6 m and assuming a fault plane dip of 75°. The fault scarp facing

Eliminato:

Eliminato: plenty

Formattato: Evidenziato

Eliminato: of structural data

Eliminato:



411 NW reaches a height of 3 m giving a heave of 0.8 m. The fault scarp located towards the  
412 southeastern part of the studied area faces SE and reaches a maximum height of 4.2 m, resulting in  
413 a heave of 1.1 m.

**Eliminato:** Both structures are quite short and developed only locally.

414 To better understanding the active deformation processes affecting the area, we also collected a  
415 series of quantitative data at 144 sites along the extension fractures, totalling 432 structural  
416 measurements (Fig. 6). The latter include: *i)* local fractures strike; *ii)* the amount of fracture dilation;  
417 *iii)* the opening direction. Opening direction values are in the range N72-163°, with a mean value of  
418 N105.7°, and most values between N90-100° (rose diagram in Fig. 6b and Fig. 7a). The fracture strike  
419 compared with the fracture opening direction, highlights a clockwise rotation of fracture strike with  
420 the increasing in opening directions (Fig. 7a). We have also quantified the local extension fracture  
421 azimuth, obtaining values between N329.8°W and N78.8°, with a peak between N0-10° and a mean  
422 value of N19.1° (rose diagram in Fig. 6b), suggesting a slight overall left-lateral component of 3.4°.  
423 More in detail, the fractures with a lateral component < 5° were here classified as pure extensional  
424 fractures, whereas the remaining fractures have a left-lateral or a right-lateral component (Fig. 7b),  
425 counting 65 fractures with a left-lateral component, 40 fractures with a right-lateral component,  
426 and 39 pure extensional fractures, out of our 144 total data. Moreover, the component of left-lateral  
427 motions (up to 52°) is larger than the right-lateral component (up to 36°). The graph of Figure 7b  
428 also shows the relation between lateral components of motions and fracture azimuth: with an  
429 increase of the fracture strike, the lateral component tends to change from the right-lateral  
430 component to the left-lateral component.

431 The dilation values measured along extension fractures are in the range of 0.07-4.14 m (Figs. 6b and  
432 7c), the average value is 0.4 m, and almost all values < 1 m. These values have been related to the  
433 local strike, showing that the greatest dilation values are associated to strike values of about N20°E;  
434 moving away from these strike values, dilation decreases gradually, especially if strike rotates in a  
435 NW-SE direction (Fig. 7e). Regarding structure length, extension fractures reach a maximum length  
436 of 93.8 m, with an average value of 13.8 m. Fractures with greater lengths show strike values  
437 between N40-60° E, decreasing gradually if strike rotates in an anticlockwise direction, and more  
438 abruptly if it rotates in a clockwise direction, as shown in Fig. 7f.

**Formattato:** Non Evidenziato

439 Regarding normal faults, we measured vertical offset every 10 meters along all the fault segments,  
440 obtaining values included in the range 0.1-7 m (Figs. 6a and 7d), the average value is 1.6 m and  
441 about half of the values < 1.5 m. Faults present greater lengths, reaching a maximum of 299.6 m,  
442 with an average value of 92.2 m (Fig. 7g). In particular, in Fig. 7g it is evident that greater lengths

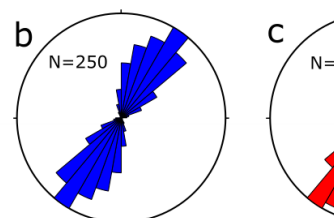
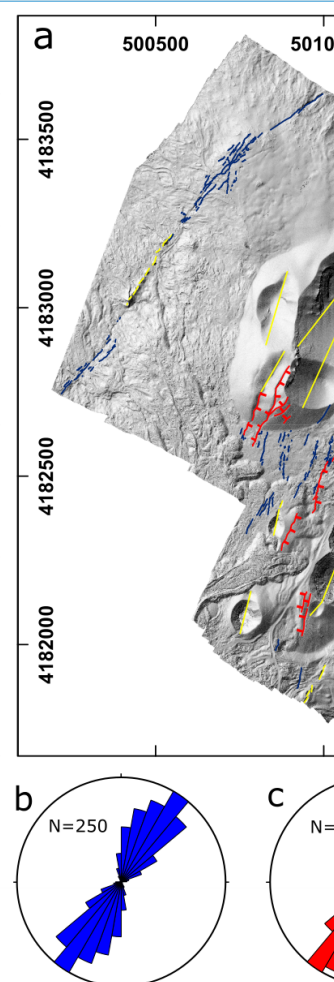
**Formattato:** Inglese americano

445 characterize SE-dipping faults, respect to NW-dipping ones, which are all < 85 m. Also, regarding the  
 446 amount of displacement, we can observe that SE-dipping faults are characterized by greater values  
 447 of offset than NW-dipping ones: the former reach a maximum offset of 7 m, whereas the latter  
 448 reach a maximum value of 3 m (Fig. 7g). Regarding length/displacement ratios for normal faults,  
 449 they are comprised between 11.3 and 284.7, with an average value of 67.9.

450 Considering a dip of 75° for normal faults, we were able to calculate the dilatational component at  
 451 both extension fractures and normal faults. Thus, we determined the total extensional component  
 452 along two transects (traces in Fig. 6a), both with a length of 1.43 km, oriented in the given overall  
 453 spreading direction, obtaining a total value of 5.3 m in the northern part of the area, and of 7.6 m  
 454 in the southern part, which correspond respectively to a stretching ratio of 1.003 in the north and  
 455 1.005 in the south.

456

Eliminato: We t



Eliminato:

Formattato: Colore carattere: Testo 1

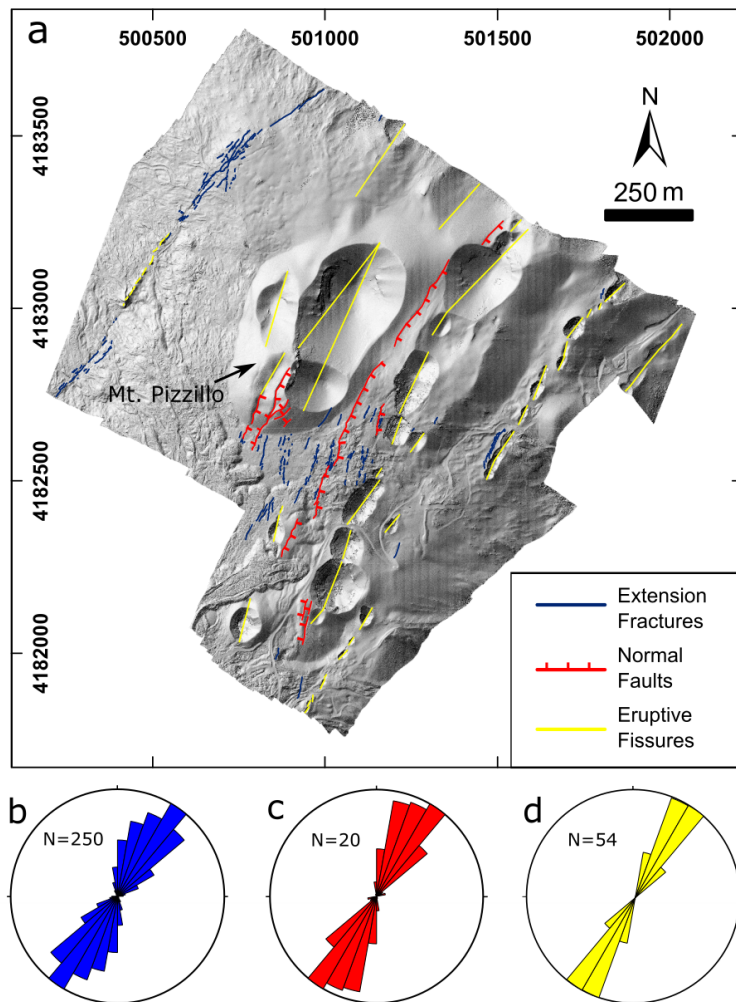


**Figure 5.** (a) Geological-structural map of the studied area, structures are traced on high-resolution SfM-derived models, reference system: UTM33N-WGS84. Location in Figure 2. Rose diagrams show the strike of the extension fractures (b), normal faults (c) and eruptive fissures (d).

Eliminato: represent

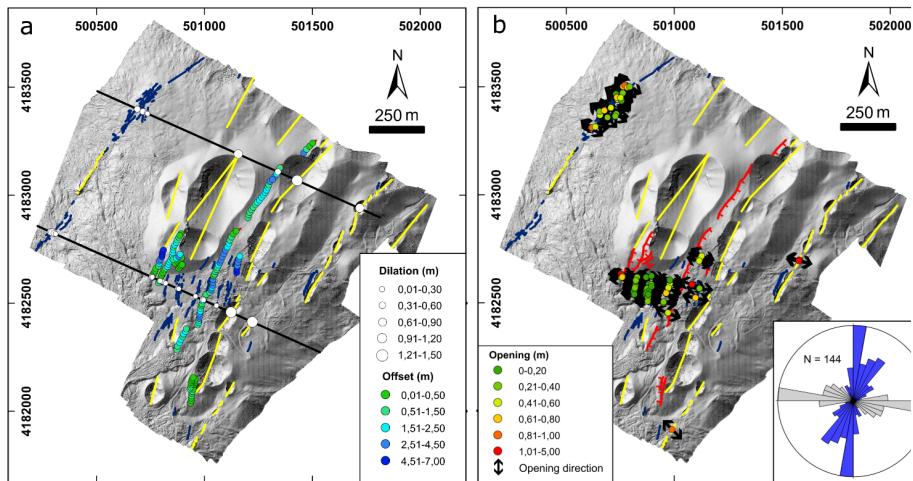
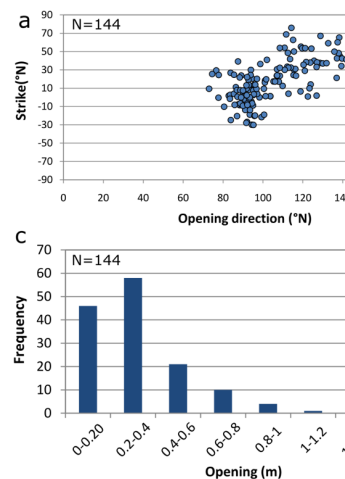
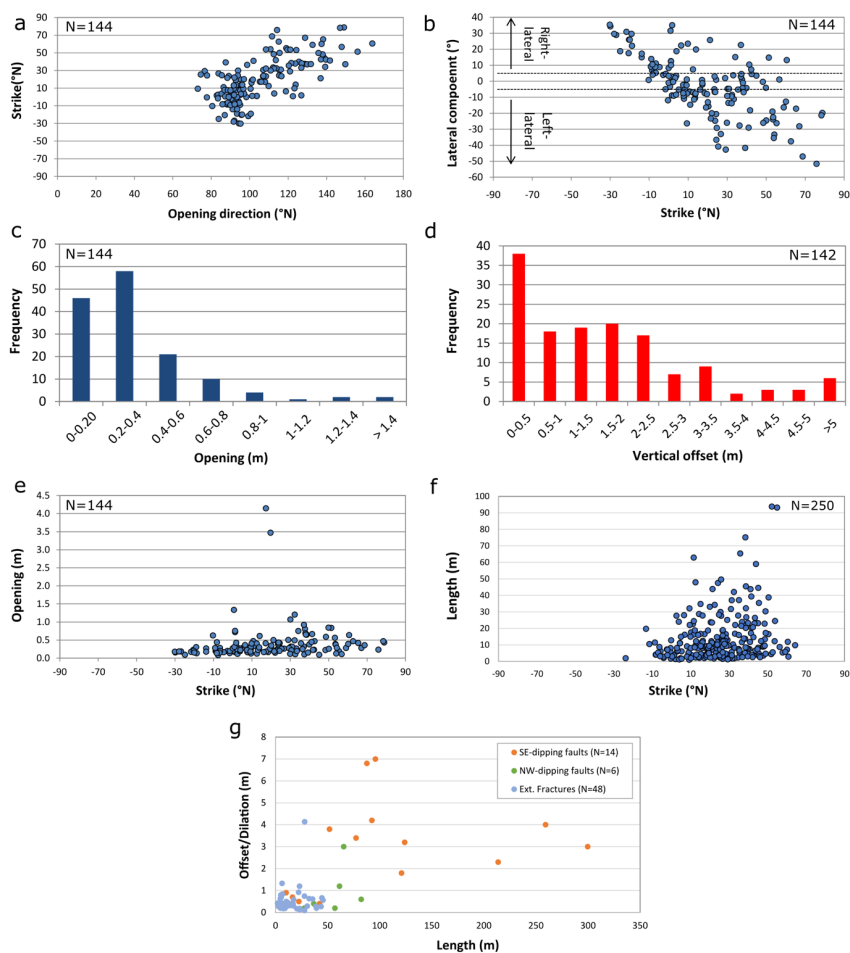


**Figure 6.** Geological-structural map showing (a) vertical offset amounts along normal faults and values of horizontal dilation measured along the two transects (black lines = traces of the transects), (b) amount of opening and opening direction in the 144 detected structural stations. Rose diagram shows the distribution of net opening direction (grey) and of the respective local fracture azimuth (blue).



Eliminato:

Formattato: Tipo di carattere: Grassetto, Corsivo, Colore  
carattere: Testo 1

Formattato: Inglese americano

**Figure 7.** (a) Graph comparing the local strike of extension fractures with the net opening direction at each site. (b) Graph comparing the local strike of extension fractures with the lateral component of motions at each site. (c) Histogram showing the frequency of the net dilation amount values measured along extension fractures. (d) Histogram showing the frequency of vertical offset values measured along normal faults. (e) Graph comparing the local strike of extension fractures with the net dilation amount at each site. (f) Graph comparing the strike of all the 250 extension fractures with their length. (g) Graph comparing the length of each structure with its maximum offset/dilation values, distinguishing between SE-dipping faults, NW-dipping faults and extension fractures.

## 5. Discussion

### 5.1. Rift geometry, structuring and kinematics



487 The part of the rift where we focused our study belongs to the 4.5-km-long NE Rift of Mt Etna, a  
 488 volcanotectonic feature that showed important volcanic and tectonic activity in historic times. The  
 489 orientation of the structures surveyed by UAVs is coherent with the remaining structures of the  
 490 central part of the NE Rift, which generally strike NE-SW. The remaining northeastern and  
 491 southwestern portions of the NE Rift show a slight clockwise and counterclockwise rotation respect  
 492 to the central part, giving to the rift a gentle concavity towards SE (Fig. 2). Most of the rift, and  
 493 similarly the studied area, is ~~dominated by~~ extension fractures and a few normal faults. Among  
 494 faults, the largest one is represented by the PF normal fault, facing SE, which constitutes the  
 495 westernmost termination of the PFS (Groppelli and Tibaldi, 1999; Tibaldi and Groppelli, 2002;  
 496 Acocella and Neri, 2005). Although the PFS has left-lateral strike-slip to transtensional motions, as  
 497 shown by the focal mechanism solutions of Figure 1, in the studied sector the PF produces an  
 498 escarpment, facing SE, about 200 m high that separates the ridge of the NE Rift from the flat plain  
 499 of Piano Provenzana. This dominant downdip motion is linked to the rotation of the PFS-PF fault  
 500 system that turns from an E-W orientation in the eastern part towards a NE-SW strike direction in  
 501 the studied area. The other faults form small grabens, one of which is present in the studied sector:  
 502 this graben is 35 m wide at the southwestern foothill of the Mt Pizzillo pyroclastic cone and widens  
 503 up to 80 m in correspondence with the upper portions of the cone. We suggest that this geometry  
 504 is mainly due to the interference between the fault dip and the shape of the conical edifice, as  
 505 observed also at Mount Laki in Iceland (Trippanera et al., 2015) or along the Harrat Lunayyir fault in  
 506 Saudi Arabia (Trippanera et al., 2019).  
 507 Regarding normal faults in the area, the calculated length/displacement ratios (11.3-284.7) are  
 508 smaller than the ones obtained by Gudmundsson et al. (2013), which are in the range 42-362  
 509 (average about 130). Anyway, our work considered a very smaller area than the one studied by  
 510 these authors, which studied all the principal faults of the eastern flank of the volcano, with lengths  
 511 up to 12,950 m and displacements up to 190 m.  
 512 The 144 opening directions measured along the extension fractures on the images obtained by  
 513 drone surveys and SfM, indicate a clear homogenous dominant extension vector trending N105.7°.  
 514 This vector is perpendicular to the largest slope of the area that is represented by the scarp of the  
 515 PF and coincides with the direction of maximum slope gradient of this part of Mt Etna (Favalli et al.,  
 516 1999). As a consequence, we retain that the opening vector of the NE Rift is strongly influenced by  
 517 gravity effects linked to the shape of the Mt Etna edifice. A comparison with seismicity indicates

**Eliminato:** characterized by the

**Eliminato:** nce of

**Formattato:** Non Evidenziato

**Formattato:** Non Evidenziato

**Eliminato:** ¶

521 that here the focal mechanism solutions have T axes trending NW-SE (Fig. 1), consistent with the  
522 opening directions measured by the drone surveys.

523 The fact that the faults dipping to the SE are longer, have larger offsets, and are more frequent than  
524 those dipping to the NW, can be linked to the fact that the NE Rift has a strongly asymmetric profile  
525 measured in a NW-SE direction. Towards NW, in fact, there is a smooth topographic decrease,  
526 whereas in the opposite direction there is the steep slope gradient produced by the PF scarp.  
527 Moreover, the northwestern side of the NE Rift is buttressed by the stable northern volcano slope,  
528 whereas the southeastern side is involved in the gravity sliding of the eastern volcano slope. This  
529 means that there is a larger gravity force acting in the SE direction.

530 The fact that most opening took place at the fractures with a strike ranging N0-50°, and that the  
531 longest fractures strike N10-55°, can be explained assuming that this range corresponds to the local  
532 orientation of the opening vector linked with the instability of the eastern volcano flank. Finally, the  
533 generally larger values of length of faults respect to fractures is compatible with the concept that  
534 extensional fractures represent an immature stage of the evolution towards faults (Gudmundsson,  
535 1987; Acocella et al., 2003; Tibaldi et al., 2019); faults can, in fact, derive from the linkage between  
536 different fracture segments during the evolutionary process.

537 Notwithstanding the general orthogonality of the opening direction respect to the average trend of  
538 the NE Rift, at a higher detail we observed that 45% of all extension fractures present a left-lateral  
539 component, whereas 27% are characterized by pure extension. Considering also that the  
540 component of left-lateral motions is larger than the right-lateral component, we conclude that the  
541 NE Rift has a left-lateral transtensional behaviour linked to the large strike-slip component of  
542 motions along the PFS.

543 Finally, we used the software “Lissage” (Lee and Angelier, 1994) and the unpublished software  
544 ATMO-STRESS, prepared in the framework of the NEANIAS project (<https://www.neanias.eu/>) of  
545 the E.U., to calculate the stress field. Lissage is a C-based software designed to reconstruct  
546 paleostress trajectories in a given area (Lee and Angelier, 1994), using as input data multiple local  
547 stress determinations, including P and T axes derived from seismological data, the direction of  
548 principal stress axes from stress inversion and any other data that describe the azimuth of  
549  $\sigma_{HMax}/Min$ . Such software can be used to reconstruct stress trajectories both using local field data  
550 and regional paleostress database (e.g. Hu et al., 1996; Munoz-Martin et al., 1998; Maestro et al.,  
551 2007; Bonali et al., 2019b). The Lissage software was here used to quantify the stress field at a  
552 broader scale by the interpolation of  $\sigma_{hmin}$  resulting from T-axes of focal mechanism solutions and

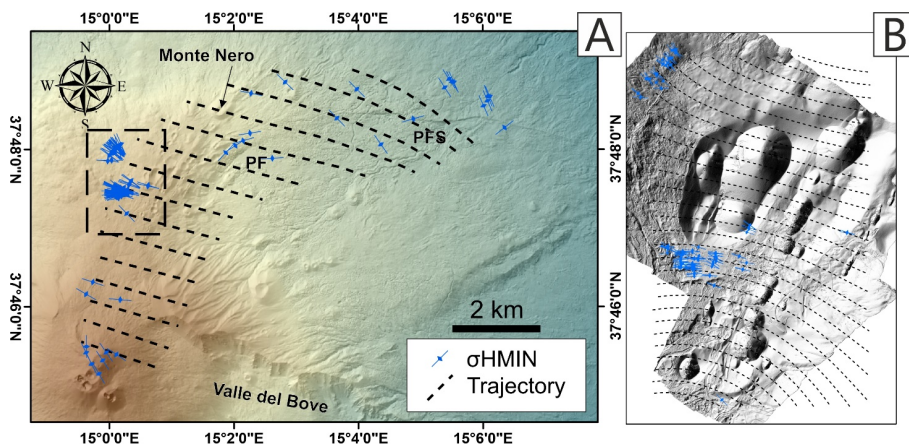
Formattato: Inglese americano

Eliminato: .....). F

Eliminato: is

555 from the single points of measurement of net dilation direction at extension fractures in our study  
 556 area (Fig. 8A), assuming that net dilation is parallel to  $\sigma_{hmin}$ . The ATMO-Stress software is the online  
 557 version of such software, and was here used to calculate in detail, at a more local scale, the stress  
 558 field based only on net dilation direction at extension fractures (Fig. 8B). Both results indicate a clear  
 559 NW-SE trend of  $\sigma_{hmin}$ , although in detail it appears a slight anticlockwise rotation from East to West.  
 560 We retain that this rotation is linked to the transition from the strike-slip dominion of the PFS, which  
 561 strikes E-W, to the more extensional dominion of the rift-PF, which strike NE-SW.

Eliminato: The ATMO-STRESS software was used



563 **Figure 8.** Stress field trajectories obtained by the interpolation of  $\sigma_{hmin}$  in the whole NE rift (A) and  
 564 in our study area (B). For stress computation, we used the program “Lissage” (Lee and Angelier,  
 565 1994) in (A), and the unpublished program ATMO-STRESS in (B).

## 568 5.2. Extensional rate

570 The total extension measured along the faults and fractures that crop out in the studied area along  
 571 the two transects, is of 5.3 m in the northern part of the area and of 7.6 m in the southern part.  
 572 Assuming the age of 1614-1624 yr AD for the oldest lavas affected by the brittle structures, we  
 573 obtain an extension rate of 1.87 cm/yr at the southern transect for the last 406 yr. Our measured  
 574 extension rates are based on a wider dataset than that published in the Tibaldi and Groppelli (2002)  
 575 paper, who indicated extension rates measured at single fractures with values of 1.8 cm/yr, 1.3  
 576 cm/yr, and 0.6 cm/yr along the rift moving from SW to NE. Our studied area corresponds to the  
 577 southwestern portion of the NE Rift that, based on the data of Tibaldi and Groppelli (2002), opens  
 578 at a higher rate. Our data thus indicate that this part of the rift opens at a slightly higher rate than

Eliminato: much more

Eliminato: ose

582 previously suggested (1.87 cm/yr instead of 1.3-1.8 cm/yr) and we retain our result is based on a  
583 more robust statistical dataset.

584 This result is also coherent with the gross general rate of deformation measured along the nearest  
585 main structure that is represented by the PFS. This fault is linked to the NE Rift and this justifies its  
586 comparison with our data. The PFS slip-rate has been quantified in its central-western part at  $0.4 \pm$   
587  $0.1$  cm/yr to  $2.2 \pm 0.1$  cm/yr, and in the eastern part at  $0.2 \pm 0.1$  cm/yr to  $0.8 \pm 0.4$  cm/yr where the  
588 PFS splays in the Vena-Presa zone (Tibaldi and Groppelli, 2002). The PFS short-term slip-rate has  
589 been assessed at 1 cm/yr in the vertical component and 2.8 cm/yr in the left-lateral component by  
590 Azzaro et al. (2001). A lower fault slip-rate of 0.6–1.5 cm/yr since 3 ka ago has been more recently  
591 calculated by D'Amato et al. (2017), although this refers only to the throw rate, not considering the  
592 strike-slip component that is especially high in the western and eastern part of the PFS. This  
593 consistency between the extension rate at the NE Rift and the slip along the PFS confirms that they  
594 accommodate the seaward sliding of the eastern volcano flank.

595

### 596 5.3. Methodological aspects

597 Results from the present work support the utility of using UAV-based SfM as a complementary tool  
598 to increase quality data collection, in addition to classical fieldwork, here aimed at defining the  
599 architecture and active processes working in a rift zone in volcanic areas. If we consider the time  
600 necessary to carry out the drone surveys, plus the time necessary to process the data and interpret  
601 them, we reach a total of 10 days of work. This yielded the collection of a huge amount of structural  
602 data, comprising 432 structural measurements (opening directions, amount of opening and local  
603 azimuth) at extension fractures. In comparison, Tibaldi and Groppelli (2002) collected just 22  
604 opening directions in the field for the same area and related structural map over a total of one week  
605 of work.

606 The use of UAVs in geoscience is quickly increasing for a series of reasons: *i)* UAV data acquisition is  
607 cheaper respect to other methods, such as Airborne and terrestrial Laser Scanning, and LiDAR  
608 (Cawood et al., 2017; Lizarazo et al., 2017); *ii)* the proposed approach reduces work-time compared  
609 to field data collection, especially in the case of study of long structures, as those of Tibaldi and  
610 Ferrari (1992), Kozhurin et al. (2006) and Trippanera et al. (2019); *iii)* the possibility to reach sites  
611 that can be inaccessible for logistic conditions or can be dangerous, such as an active volcano.  
612 Moreover, the excellent accuracy of the SfM-derived models allows us to carry out observations  
613 and measures at details in the order of cm, thus a scale that is comparable to field surveys. This

Eliminato: for massive high

Eliminato: such approach allows to save plenty of time with respect

Eliminato: specifically

Eliminato: in broad areas or at long

Eliminato: , such

Eliminato: and

621 scale, together with the velocity of the workflow and related processing, can even improve  
622 performance.

623 Furthermore, the rapid development of UAVs technology (furnished with Real-time kinematic  
624 positioning system) will increase the accuracy of the SfM outputs in the future, flying also at a higher  
625 elevation from the ground. Similarly, also the UAV flight stability, camera quality and battery  
626 capacity can improve thanks to the continuous delivery of new UAVs and related items.

627 In regard to limitations arising from the use of the UAV-based SfM, we mention the dependence on  
628 the flight time that is linked to the battery life, weather conditions, flight rules, and the fundamental  
629 step of placing and surveying the GCPs. The latter are needed to precisely scale and reference the  
630 model, but their placement is time consuming, slowing down the total time needed for the UAV  
631 missions, particularly over broad areas. Smith et al. (2016) suggested to consider a minimum 3  
632 GCPs, whereas other authors considered a higher number of GCPs, but decreasing the overlap ratio  
633 among the pictures to 60-70% (Javernick et al., 2014). Finally, increasing overlap ratio, it is possible  
634 to decrease the number of GCPs considered for scaling and referencing (Esposito et al., 2017).

635

## 636 **6. Conclusions**

637 We applied UAV-based Structure-from-Motion (SfM) photogrammetry to analyze a high-altitude  
638 area characterized by rough terrains in the northeastern part of Mt Etna. The area is affected by the  
639 presence of the NE Rift, a volcano-tectonic feature composed of NE-striking historic eruptive  
640 fissures, extension fractures and normal faults. The stratigraphic deposits span in age from  $56.6 \pm$   
641  $15.4$  ka BP to nowadays, whereas in the area surveyed by the drones, the deposits are mostly  
642 historic in age.

643 The highly detailed drone survey, in the order of 2.8 cm of resolution, showed that the studied  
644 sector of the NE Rift is affected by 250 extension fractures, 20 normal fault segments, and 54  
645 eruptive fissures. The extension fractures strike mainly N20-50°, with an average strike of N24.6°.  
646 The normal faults strike mainly N10-40° with an average strike of N25.3°. The eruptive fissures strike  
647 mainly N20-40° with an average strike of N29.8°.

648 We measured 432 structural data, comprising local fracture strike, dilation amount, and opening  
649 direction. Opening direction values are in the range N72-163°, with a mean value of N105.7°. A  
650 comparison respect to fracture strike indicates the presence of a slight overall left-lateral  
651 component of 3.4°. Moreover, 65 fractures have a left lateral component, 40 fractures a right lateral  
652 component and 39 pure extension. The component of left-lateral motions (up to 52°) is larger than



the right-lateral component (up to 36°). These data suggest the effect of the left-lateral normal Pernicana Fault System on the NE Rift kinematics.

Seismicity seems to be concentrated along the Pernicana-Piano Provenzana faults, whereas earthquake focal mechanism solutions show T-axes trending perpendicularly to the NE Rift, consistent with the results of our measurements of dilation orientations.

Assuming the age of 1614-1624 yr AD for the oldest lavas affected by the studied fractures, we obtain an extension rate of 1.87 cm/yr for the last 406 yr. This rate is consistent with the data measured by other authors at the Pernicana Fault System.

Results indicate that SfM photogrammetry coupled with drone surveys allows to collect large data sets with a detail comparable to field surveys. Drone survey has the advantage of collecting more data in the same time period respect to classical fieldwork, and also allows data collection in difficult terrains where logistics can represent an insurmountable obstacle.

**Data availability:**

Data are available from the corresponding author upon request.

**Author contribution:**

Conceptualization of the project was done by TA and CN. Photogrammetry processing of the 3D model was done by BFL. Data for the model and its calibration were collected and provided by CM, DBE, BFL and FL. Geological structural data and stratigraphy have been prepared by NM. Seismological data and text come from FS and LH. Evaluation of the model results and their interpretation were performed by CN and BFL. TA wrote the paper with help from all co-authors. All authors read and approved the final paper.

**Competing interests:**

The authors declare that they have no conflict of interest.

**Acknowledgments:** We acknowledge R. E. Rizzo and D. Tripanera for their useful suggestions to improve an earlier version of the manuscript. We are grateful to Tiziana Tuvè (INGV) for the data on hypocentral location of earthquakes in 2002-2003, and to Luciano Scarfi and Carmelo Cassisi for the access to [http://sismoweb.ct.ingv.it/maps/eq\\_maps/focals/index.php](http://sismoweb.ct.ingv.it/maps/eq_maps/focals/index.php). This study has been

Codice campo modificato

conducted in the framework of the [EU project NEANIAS, within which the software ATMO-stress has been developed under the guidance of K. Karantzas, the International Lithosphere Program - Task Force II \(Leader A. Tibaldi\)](#), and it is also an outcome of: *i)* Project MIUR – Dipartimenti di Eccellenza 2018–2022; *ii)* GeoVires, the Virtual Reality Lab for Earth Sciences, Department of Earth and Environmental Sciences, University of Milan Bicocca, Italy (<https://geovires.unimib.it/>). [We also acknowledge the Parco dell’Etna \(<https://parcoetna.it/>\) for permission for drone surveys.](#)

## References

- Acocella, V., Neri, M. (2003). What makes flank eruptions? The 2001 Etna eruption and the possible triggering mechanisms. *Bull. Volcanol.*, 65: 517-529, DOI: 10.1007/s00445-003-0280-3.
- Acocella, V., Neri, M. (2005). Structural features of an active strike-slip fault on the sliding flank of Mt. Etna (Italy). *J. Structural Geology*, 27/2, pp. 343-355, doi: 10.1016/j.jsg.2004.07.006.
- Acocella V., Neri M. (2009). Dike propagation in volcanic edifices: overview and possible developments, Special Issue: Gudmundsson – Volcanoes, *Tectonophysics*, 471, 67-77, doi: 10.1016/j.tecto.2008.10.002.
- [Acocella, V., Korme, T., Salvini, F., 2003. Formation of normal faults along the axial zone of the Ethiopian Rift. \*J. Struct. Geol.\*, 25, 503–513.](#)
- Acocella V., Neri M., Sulpizio R. (2009). Dike propagation within active central volcanic edifices: constraints from Somma-Vesuvius, Etna and analogue models. *Bull. Volcanol.*, 71:219–223, DOI 10.1007/s00445-008-0258-2.
- Acocella V., Neri M., Norini G., (2013). An overview of analogue models to understand a complex volcanic instability: application to Etna, Italy, *J. Volcanol. Geotherm. Res.*, 251, 98–111, doi:10.1016/j.jvolgeores.2012.06.003.
- [Acocella, V., Neri, M., Behncke, B., Bonforte, A., del Negro, C., & Ganci, G. \(2016\). Why does a mature volcano need new vents? The case of the New Southeast Crater at Etna. \*Frontiers in Earth Science\*, 4, 67. <https://doi.org/10.3389/feart.2016.00067>.](#)
- [Alparone, S., A. Bonaccorso, A. Bonforte, and G. Currenti \(2013a\). Long-term stress-strain analysis of volcano flank instability: The eastern sector of Etna from 1980 to 2012, \*J. Geoph. Res.\*, 118, 5098–5108, doi:10.1002/jgrb.50364, 2013.](#)
- Alparone, S., O. Cocina, S. Gambino, A. Mostaccio, S. Spampinato, T. Tuvè, A. Ursino, 2013b. Seismological features of the Pernicana–Provenzana Fault System (Mt. Etna, Italy) and implications for the dynamics of northeastern flank of the volcano. *J. Volcanol. Geoth. Res.*, 251, 16–26, <https://doi.org/10.1016/j.jvolgeores.2012.03.010>.
- Antoniou, V., Nomikou, P., Bardouli, P., Sorotou, P., Bonali, F., Ragia, L., Metaxas, A., 2019. The story map for Metaxa mine (Santorini, Greece): a unique site where history and volcanology meet each other. In *Proceedings of the 5th International Conference on Geographical Information Systems Theory, Applications and Management*, Heraklion, Greece, 3-5 May 2019; SciTePress, 1, 212–219.
- Apuani T., C. Corazzato, A. Merri, & Tibaldi, A. (2013). Understanding Etna flank instability through numerical models, *Journal of Volcanology and Geothermal Research*, 251, 112–126, doi: <https://doi.org/10.1016/j.jvolgeores.2012.06.015>.
- Azzaro, R. (2004). Seismicity and active tectonics in the Etna region: constraints for a seismotectonic model, in *Mt. Etna: volcano laboratory*, Geophysical monograph (eds. A. Bonaccorso, S. Calvari,

Formattato: Inglese americano

Eliminato: ¶

Formattato: Italiano

Formattato: Inglese americano

729 M. Coltelli, C. Del Negro, S. Falsaperla), AGU, Washington D.C., 143, 205–220,  
730 doi:10.1029/143GM13.

731 Azzaro, R., L. Ferrelì, A. L. Michetti, L. Serva, and E. Vittori (1998). Environmental hazard of capable  
732 faults: the case of the Pernicana fault (Mt. Etna, Sicily), *Nat. Hazards*, 17, 147–162.

733 Azzaro, R., Mattia, M., & Puglisi, G. (2001). Fault creep and kinematics of the eastern segment of the  
734 Pernicana Fault (Mt. Etna, Italy) derived from geodetic observations and their tectonic  
735 significance. *Tectonophysics*, 333(3–4), 401–415.

736 Behncke, B., Branca, S., Corsaro, R.A., De Beni, E., Miraglia, L. and Proietti, C. (2014). The 2011–2012  
737 summit activity of Mount Etna: birth, growth and products of the new SE crater. *J. Volcanol.*  
738 *Geotherm. Res.* 270, 10–21.

739 Benassi, F., Dall’Asta, E., Diotri, F., Forlani, G., Morra di Cella, U., Roncella, R., Santise, M. (2017).  
740 Testing accuracy and repeatability of UAV blocks oriented with gnss-supported aerial  
741 triangulation. *Remote Sens.*, 9, 172.

742 Bonali, F. L., Corazzato, C., & Tibaldi, A. (2011). Identifying rift zones on volcanoes: an example from  
743 La Réunion island, Indian Ocean. *Bulletin of volcanology*, 73(3), 347–366.

744 Bonali, F. L., Tibaldi, A., Marchese, F., Fallati, L., Russo, E., Corselli, C., Savini, A. (2019a). UAV-based  
745 surveying in volcano-tectonics: An example from the Iceland rift. *J. Struct. Geol.*, 121, 46–64.

746 Bonali, F. L., Tibaldi, A., Mariotto, F. P., Saviano, D., Meloni, A., & Sajovitz, P. (2019b). Geometry,  
747 oblique kinematics and extensional strain variation along a diverging plate boundary: The  
748 example of the northern Theistareykir Fissure Swarm, NE Iceland. *Tectonophysics*, 756, 57–72.

749 Bonali, F. L., Tibaldi, A., Corti, N., Fallati, L., & Russo, E. (2020). Reconstruction of Late Pleistocene-  
750 Holocene Deformation through Massive Data Collection at Krafla Rift (NE Iceland) Owing to  
751 Drone-Based Structure-from-Motion Photogrammetry. *Applied Sciences*, 10(19), 6759.

752 Bonforte, A., Guglielmino, F., Coltelli, M., Ferretti, A., & Puglisi, G. (2011). Structural assessment of  
753 Mount Etna volcano from Permanent Scatterers analysis. *Geochemistry, Geophysics,*  
754 *Geosystems*, 12, Q02002. <https://doi.org/10.1029/2010GC003213>.

755 Borgia, A., Ferrari, L., & Pasquarè, G. (1992). Importance of gravitational spreading in the tectonic  
756 and volcanic evolution of Mount Etna. *Nature*, 357(6375), 231–235.

757 Branca S., Coltelli M. & Groppelli G. (2011). Geological evolution of a complex basaltic stratovolcano:  
758 Mount Etna, Italy. *It. J. Geosci. (Boll. Soc. Geol. It.)*, 130 (3), doi: 10.3301/IJG.2011.13.

759 Brunier, G., Fleury, J., Anthony, E. J., Gardel, A., Dussouillez, P. (2016). Close-range airborne  
760 Structure-from-Motion Photogrammetry for high-resolution beach morphometric surveys:  
761 Examples from an embayed rotating beach. *Geomorphology*, 261, 76–88.

762 Burns, J.H.R., Delparte, D. (2017). Comparison of commercial structure-from-motion  
763 photogrammetry software used for underwater three-dimensional modeling of coral reef  
764 environments. In: *International Archives of the Photogrammetry, Remote Sensing and Spatial*  
765 *Information Sciences; ISPRS Archives*, 42, 127–131.

766 Cappello, A., Neri, M., Acocella, V., Gallo, G., Vicari, A., Del Negro, C. (2012). Spatial vent opening  
767 probability map of Mt. Etna volcano (Sicily, Italy), *Bull. Volcanol.*, 74, 2083–2094, doi:  
768 10.1007/s00445-012-0647-4.

769 Cawood, A.J., Bond, C.E., Howell, J.A., Butler, R.W., Totake, Y., 2017. LiDAR, UAV or compass-  
770 clinometer? Accuracy, coverage and the effects on structural models. *J. Struct. Geol.*, 98, 67–82.

771 Chu, D.; Gordon, R. G., 1999. Evidence for motion between Nubia and Somalia along the Southwest  
772 Indian Ridge. *Nature*, 398, 64–67, doi:10.1038/18014.

773 Cocina, O., Neri, G., Privitera, E., & Spampinato, S. (1997). Stress tensor computations in the Mount  
774 Etna area (Southern Italy) and tectonic implications. *Journal of Geodynamics*, 23(2), 109–127.

Formattato: Inglese americano

Formattato: Inglese americano

Eliminato:

776 Cocina, O., Neri, G., Privitera, E., & Spampinato, S. (1998). Seismogenic stress field beneath Mt. Etna  
777 (South Italy) and possible relationships with volcano-tectonic features. *Journal of volcanology*  
778 and geothermal research, 83(3-4), 335-348.

779 Coltelli, M., Garduño, V.H., Neri, M., Pasquarè, G. & Pompilio, M. (1994). Geology of northern wall  
780 of Valle del Bove, Etna (Sicily). *Acta Vulcanol.*, 5, 55-68.

781 Coltelli M., Del Carlo P. & Vezzoli L. (2000). Stratigraphic constrains for explosive activity in the last  
782 100 ka at Etna volcano. Italy. *Inter. J. Earth Sciences*, 89, 665-677.

783 Condomines, M., Tanguy, J. C., Kieffer, G. & Allegre, C. J. (1982). Magmatic evolution of a volcano  
784 studied by 230Th-238U disequilibrium and trace elements systematics: the Etna case.  
785 *Geochimica et Cosmochimica Acta*, 46, 1397-1416. Pergamon Press Ltd. U.S.A.

786 Cook, K.L. (2017). An evaluation of the effectiveness of low-cost UAVs and structure from motion  
787 for geomorphic change detection. *Geomorphology*, 278, 195-208.

788 Cortesi, C., Fornaseri, M., Romano, R., Alessio, M., Allegri, L., Azzi, C., Bella, F., Calderoni, G., Follieri,  
789 M., Improta, S., Magri, D., Preite, Martinez M., Sadori, L., Petrone, V. & Turi, B. (1988).  
790 Cronologia 14C di piroclastiti recenti del Monte Etna identificazione e distribuzione dei fossili  
791 vegetali. *Boll. Soc. Geol. It.*, 107, 531-545.

792 D'amato, D., Pace, B., Di Nicola, L., Stuart, F. M., Visini, F., Azzaro, R., Branca, S. & Barfod, D. N.  
793 (2017). Holocene slip rate variability along the Pernicana fault system (Mt. Etna, Italy): Evidence  
794 from offset lava flows. *GSA Bulletin*, 129(3-4), 304-317.

795 [Darmawan, H., Walter, T.R., Brotopuspito, K.S., Nandaka, I.G.M.A. \(2018\). Morphological and](#)  
796 [structural changes at the Merapi lava dome monitored in 2012-15 using unmanned aerial](#)  
797 [vehicles \(UAVs\). \*J. Volcanol. Geotherm. Res.\*, 349, 256-267.](#)

798 De Beni E., Branca S., Coltelli M., Groppelli G. & Wijbrans J. (2011). 40Ar/39Ar isotopic dating of Etna  
799 volcanic succession. *It. J. Geosci. (Boll. Soc. Geol. It.)*, 130 (3), 292-305, doi:  
800 10.3301/IJG.2011.14.

801 [De Beni, E., Cantarero, M., Messina, A. \(2019\). UAVs for volcano monitoring: A new approach](#)  
802 [applied on an active lava flow on Mt. Etna \(Italy\), during the 27 February-02 March 2017](#)  
803 [eruption. \*J. Volcanol. Geotherm. Res.\*, 369, 250-262.](#)

804 De Novellis, V., Atzori, S., De Luca, C., Manzo, M., Valerio, E., Bonano, M., C. Cardaci, R. Castaldo, D.  
805 Di Bucci, M. Manunta, G. Onorato, S. Pepe, G. Solaro, P. Tizzani, J. Zinno, M. Neri, R. Lanari, F.  
806 Casuet (2019). DInSAR analysis and analytical modeling of Mount Etna displacements: The  
807 December 2018 volcano-tectonic crisis. *Geophysical Research Letters*, 46,  
808 doi.org/10.1029/2019GL082467.

809 Del Negro C., Cappello A., Neri M., Bilotta G., Héroult A., Ganci G. (2013). Lava flow hazards at Etna  
810 volcano: constraints imposed by eruptive history and numerical simulations, *Scientific Reports*  
811 - *Nature*, 3:3493, doi: 10.1038/srep03493.

812 Esposito, G., Mastroiocco, G., Salvini, R., Oliveti, M., Starita, P. (2017). Application of UAV  
813 photogrammetry for the multi-temporal estimation of surface extent and volumetric  
814 excavation in the Sa Pigada Bianca open-pit mine, Sardinia, Italy. *Environ. Earth Sci.*, 76, 103.

815 Fallati, L., Saponari, L., Savini, A., Marchese, F., Corselli, C., Galli, P. (2020). Multi-Temporal UAV Data  
816 and Object-Based Image Analysis (OBIA) for Estimation of Substrate Changes in a Post-Bleaching  
817 Scenario on a Maldivian Reef. *Remote Sens.*, 12, 2093.

818 Favalli, M., Innocenti, F., Teresa Pareschi, M., Pasquarè, G., Mazzarini, F., Branca, S., & Tibaldi, A.  
819 (1999). The DEM of Mt. Etna: geomorphological and structural implications. *Geodinamica Acta*,  
820 12(5), 279-290.

821 Garduño V.H., Neri M., Pasquarè G., Borgia A., Tibaldi A., 1997. Geology of the NE-Rift of Mount  
822 Etna (Sicily, Italy). *Acta Vulcanologica*, 9, (1/2), 91-100.

Eliminato:

Formattato: Inglese (Regno Unito)

Formattato: Tipo di carattere: Non Corsivo

Formattato: Inglese (Regno Unito)

Formattato: Tipo di carattere: Non Corsivo

Formattato: Tipo di carattere: Non Corsivo

Eliminato:

Eliminato:

Eliminato:

Eliminato:

Eliminato:

Eliminato:

Eliminato:

Eliminato:

Eliminato:

Eliminato:

Eliminato:

Eliminato:

Gerloni, I.G., Carchiolo, V., Vitello, F.R., Sciacca, E., Becciani, U., Costa, A., Riggi, S., Bonali, F.L., Russo, E., Fallati, L., Marchese, F., Tibaldi, A. (2018). Immersive Virtual Reality for Earth Sciences. In: Proceedings of the 2018 Federated Conference on Computer Science and Information Systems (FedCSIS) IEEE, Poznan, Poland, 9-12 September 2018, 527-534.

Geshi N. and Neri M. (2014). Dynamic feeder dyke systems in basaltic volcanoes: the exceptional example of the 1809 Etna eruption (Italy). *Front. Earth Sci.* 2:13. doi: 10.3389/feart.2014.00013.

Gillot, P.Y., Kieffer, G. & Romano, R. (1994). The evolution of Mount Etna in the light of potassium-argon dating. *Acta Vulcanol.*, 5, 81-87.

Groppelli, G., and Tibaldi, A. (1999). Control of rock rheology on deformation style and slip-rate along the active Pernicana Fault, Mt. Etna, Italy. *Tectonophysics*, 305(4), 521– 537. doi.org/10.1016/S0040-1951(99)00035-9.

Guardo, R. A., De Siena, L., & Dreidemie, C. (2020). Mt. Etna feeding system and sliding flank: a new 3D image from earthquakes distribution in a customisable GIS. *Front. Earth Sci.*, 8:589925, doi: 10.3389/feart.2020.589925

Gudmundsson, A. (1987). Geometry, formation and development of tectonic fractures on the Reykjanes Peninsula, southwest Iceland. *Tectonophysics*, 139, 295–308.

Gudmundsson, A., De Guidi, G., Scudero, S. (2013). Length–displacement scaling and fault growth. *Tectonophysics*, 608, 1298-1309.

Gwinner, K., Coltelli, M., Flohrer, J., Jaumann, R., Matz, K. D., Marsella, M., Roatsch T., Scholten F., Trauthan, F. (2006). The HRSC-AX Mt. Etna project: High-resolution orthoimages and 1 m DEM at regional scale. *International Archives of Photogrammetry and Remote Sensing*, XXXVI (Part 1), <http://isprs.free.fr/documents/Papers/T05-23>.

Hu, J. C., Angelier, J., Lee, J. C., Chu, H. T., & Byrne, D. (1996). Kinematics of convergence, deformation and stress distribution in the Taiwan collision area: 2-D finite-element numerical modelling. *Tectonophysics*, 255(3-4), 243-268.

James, M. R., Robson, S. (2012). Straightforward reconstruction of 3D surfaces and topography with a camera: accuracy and geoscience application. *J. Geophys. Res. Earth Surf.*, 117, F03017, doi: 10.1029/2011JF002289.

James, M.R., Robson, S., d'Oleire-Oltmanns, S., Niethammer, U. (2017). Optimising UAV topographic surveys processed with structure-from-motion: ground control quality, quantity and bundle adjustment. *Geomorphology*, 280, 51-66.

Javernick, L., Brasington, J., Caruso, B. (2014). Modeling the topography of shallow braided rivers using Structure-from-Motion photogrammetry. *Geomorphology*, 213, 166–182.

Jestin, F., Huchon, P., Gaulier, J. M. (1994). The Somalia plate and the East-African Rift system—Present-day kinematics. *Geophys. J. Int.*, 116, 637–654, doi:10.1111/j.1365-246X.1994.tb03286.x.

Keir, D., Ebinger, C. J., Stuart, G. W., Daly, E., Ayele, A. (2006). Strain accommodation by magmatism and faulting as rifting proceeds to breakup: Seismicity of the northern Ethiopian rift. *J. Geophys. Res. Solid Earth*, 111, B05314, doi:10.1029/2005JB003748.

Kozhurin, A., Acocella, V., Kyle, P. R., Lagmay, F. M., Melekestsev, I. V., Ponomareva, V., Rust D., Tibaldi A., Tunesi A., Corazzato C., Rovida A., Sakharovh A., Tengonciang A., Uyd H. (2006). Trenching studies of active faults in Kamchatka, eastern Russia: Palaeoseismic, tectonic and hazard implications. *Tectonophysics*, 417(3-4), 285-304.

Lanzafame, G., Neri, M., Coltelli, M., Lodato, L., & Rust, D. (1997). North-South compression in the Nit. Etna region (Sicily): spatial and temporal distribution. *Acta Vulcanologica*, 9, 121-134.

Lee, J. C., & Angelier, J. (1994). Paleostress trajectory maps based on the results of local determinations: the “Lissage” program. *Computers & Geosciences*, 20(2), 161-191.

Formattato: Inglese americano

Eliminato: ¶



884 Lizarazo, I., Angulo, V., Rodríguez, J. (2017). Automatic mapping of land surface elevation changes  
885 from UAV-based imagery. *Int. J. Remote Sens.*, 38, 2603–2622.

886 Lomax, A., J. Virieux, P. Volant, and C. Thierry-Berge (2000). Probabilistic earthquake location in 3D  
887 and layered models, in *Advances in Seismic Event Location*, C. H. Thurber and N. Rabinowitz  
888 (Editors), Kluwer Academic Publishers, Dordrecht/Boston/London, 101–134.

889 Lyakhovsky, V., Segev, A., Schattner, U., Weinberger, R., 2012. Deformation and seismicity  
890 associated with continental rift zones propagating toward continental margins. *Geochem.*  
891 *Geophys. Geosyst.*, 13, Q01012, doi:10.1029/2011GC003927.

892 Maestro, A., Somoza, L., Rev, J., Martínez-Frías, J., & López-Martínez, J. (2007). Active tectonics, fault  
893 patterns, and stress field of Deception Island: a response to oblique convergence between the  
894 Pacific and Antarctic plates. *Journal of South American Earth Sciences*, 23(2-3), 256-268.

895 Mattia, M., Bruno, V., Caltabiano, T., Cannata, A., Cannavò, F., D'Alessandro, W., di Grazia, G.,  
896 Federico, C., Giammanco, S., la Spina, A., Liuzzo, M., Longo, M., Monaco, C., Patanè, D., &  
897 Salerno, G. (2015). A comprehensive interpretative model of slow slip events on Mt. Etna's  
898 eastern flank. *Geochemistry, Geophysics, Geosystems*, 16, 635–658.  
899 <https://doi.org/10.1002/2014GC005585>.

900 Mostaccio, A., T. Tuvè, D. Patanè, G. Barberi, and L. Zuccarello (2013). Improving Seismic  
901 Surveillance at Mt. Etna Volcano by Probabilistic Earthquake Location in a 3D Model 103, 4,  
902 2447–2459, doi: 10.1785/0120110202.

903 Müller, D., Walter, T.R., Schöpa, A., Witt, T., Steinke, B., Gudmundsson, M.T., Dürig, T. (2017). High-  
904 resolution digital elevation modeling from TLS and UAV campaign reveals structural complexity  
905 at the 2014/2015 Holuhraun eruption site, Iceland. *Front. Earth Sci.*, 5, 59.

906 Munoz-Martin, A., Cloetingh, S. A. P. L., De Vicente, G., & Andeweg, B. (1998). Finite-element  
907 modelling of Tertiary paleostress fields in the eastern part of the Tajo Basin (central Spain).  
908 *Tectonophysics*, 300(1-4), 47-62.

909 Neri M., Acocella V., Behncke B. (2004). The role of the Pernicana Fault System in the spreading of  
910 Mount Etna (Italy) during the 2002-2003 eruption. *Bull Volcanol*, 66, 417-430, DOI:  
911 10.1007/s00445-003-0322-x.

912 Neri M., Acocella V., Behncke B., Maiolino V., Ursino A. Velardita R. (2005). Contrasting triggering  
913 mechanisms of the 2001 and 2002-2003 eruptions of Mount Etna (Italy). *J. Volcanol. Geotherm.*  
914 *Res.*, 144, 235-255, doi:10.1016/j.jvolgeores.2004.11.025.

915 Neri M., Acocella V., Behncke B., Giammanco S., Mazzarini F., Rust D. (2011). Structural analysis of  
916 the eruptive fissures at Mount Etna (Italy). *Ann. Geophys.*, 54, 5, 464-479, doi: 10.4401/ag-  
917 5332.

918 Patanè, D., O. Cocina, S. Falsaperla, E. Privitera, and S. Spampinato (2004). Mt. Etna volcano: A  
919 seismological framework, in *Mt. Etna Volcano Laboratory*, A. Bonaccorso, S. Calvari, M. Coltelli,  
920 C. Del Negro, Falsaperla (Editors), *American Geophysical Monograph* 143, 147–165, AGU,  
921 Washington, D. C., <https://doi.org/10.1029/143GM10>.

922 Ruch J., V. Acocella, F. Storti, M. Neri, S. Pepe, G. Solaro, E. Sansosti (2010). Detachment depth of  
923 an unstable volcano revealed by rollover deformation: an integrated approach at Mt. Etna,  
924 *Geophys. Res. Lett.*, 37, L16304, doi:10.1029/2010GL044131.

925 Ruch J., Pepe S., Casu F., Acocella V., Neri M., Solaro G., Sansosti E. (2012). How do rift zones relate  
926 to volcano flank instability? Evidence from collapsing rifts at Etna, *Geophys. Res. Lett.*, 39,  
927 L20311, doi:10.1029/2012GL053683.

928 Ruch J., Pepe S., Casu F., Solaro G., Pepe A., Acocella V., Neri M., Sansosti E. (2013). Seismo-tectonic  
929 behavior of the Pernicana Fault System (Mt Etna): a gauge for volcano flank instability? *J.*  
930 *Geophys. Res. Solid Earth*, 118, 4398–4409, doi:10.1002/jgrb.50281.

931 Salvador A. (1994). *International Stratigraphic Guide*. GSA Salvador A. (Ed.), Boulder, 1-214.

Formattato: Inglese (Regno Unito)

Formattato: Inglese americano

Formattato: Inglese (Regno Unito)

Formattato: Inglese americano

Formattato: Inglese (Regno Unito)

932 Scarfi, L., A. Messina, C. Cassisi (2013). Sicily and Southern Calabria focal mechanism database: a  
 933 valuable tool for the local and regional stress field determination, *Ann. Geophys.*, 56, 1, D0109;  
 934 doi:10.4401/ag-6109.

935 Siniscalchi A., Tripaldi S., Neri M., Balasco M., Romano G., Ruch J., Schiavone D. (2012). Flank  
 936 instability structure of Mt Etna inferred by a magnetotelluric survey, *J. Geophys. Res.*, 117,  
 937 B03216, doi:10.1029/2011JB008657, 2012.

938 Smith, M.W., Carrivick, J.L., Quincey, D.J. (2016). Structure from motion photogrammetry in physical  
 939 geography. *Prog. Phys. Geogr.*, 40, 247–275.

940 Solaro G., Acocella V., Pepe S., Ruch J., Neri M., Sansosti E. (2010). Anatomy of an unstable volcano  
 941 through InSAR data: multiple processes affecting flank instability at Mt. Etna in 1994–2008. *J.*  
 942 *Geophys. Res.*, 115, B10405, doi:10.1029/2009JB000820.

943 Tibaldi, A. (1995). Morphology of pyroclastic cones and tectonics. *Journal of Geophysical Research:*  
 944 *Solid Earth*, 100(B12), 24521–24535.

945 Tibaldi, A., & Ferrari, L. (1992). Latest Pleistocene-Holocene tectonics of the Ecuadorian Andes.  
 946 *Tectonophysics*, 205(1-3), 109–125.

947 Tibaldi, A., & Groppelli, G. (2002). Volcano-tectonic activity along structures of the unstable NE flank  
 948 of Mt. Etna (Italy) and their possible origin. *Journal of Volcanology and Geothermal Research*,  
 949 115(3-4), 277–302.

950 Tibaldi, A., & Bonali, F. L. (2017). Intra-arc and back-arc volcano-tectonics: Magma pathways at  
 951 Holocene Alaska-Aleutian volcanoes. *Earth-Science Reviews*, 167, 1–26.

952 Tibaldi, A., Bonali, F. L., Mariotto, F. P., Russo, E., & Tenti, L. R. (2019). The development of divergent  
 953 margins: Insights from the North Volcanic Zone, Iceland. *Earth and Planetary Science Letters*,  
 954 509, 1–8.

955 Tibaldi, A., Bonali, F. L., Vitello, F., Delage, E., Nomikou, P., Antoniou, V., Becciani U., Van Wyk de  
 956 Vries B., Krokos M., Whitworth, M. (2020). Real world-based immersive Virtual Reality for  
 957 research, teaching and communication in volcanology. *Bull. Volcanol.*, 82, 38.

958 Trippanera, D., Ruch, J., Acocella, V., Rivalta, E. (2015). Experiments of dike-induced  
 959 deformation: insights on the long-term evolution of divergent plate boundaries. *J. Geophys.*  
 960 *Res. Solid Earth*, 120(10), 6913–6942.

961 Trippanera, D., Ruch, J., Passone, L., Jónsson, S. (2019). Structural mapping of dike-induced faulting  
 962 in Harrat Lunayyir (Saudi Arabia) by using high resolution drone imagery. *Front. Earth Sci.*, 7,  
 963 168.

964 Turner, D., Lucieer, A., Watson, C. (2012). An automated technique for generating georectified  
 965 mosaics from ultra-high resolution unmanned aerial vehicle (UAV) imagery, based on structure  
 966 from motion (SfM) Point clouds. *Remote Sens.*, 4, 1392–1410.

967 Urulaub, M., Petersen, F., Gross, F., Bonforte, A., Puglisi, G., Guglielmino, F., Krastel, S., Lange, D., &  
 968 Kopp, H. (2018). Gravitational collapse of Mount Etna's southeastern flank. *Science Advances*,  
 969 4(10), eaat9700. <https://doi.org/10.1126/sciadv.aat9700>.

970 Verhoeven, G. (2011). Taking computer vision aloft—archaeological three-dimensional  
 971 reconstructions from aerial photographs with photostan. *Archaeol. Prospect.*, 18, 67–73.

972 Villani, F., Pucci, S., Azzaro, R., Civico, R., Cinti, F. R., Pizzimenti, L., G. Tarabusi, S. Branca, C. A.  
 973 Brunori, M. Caciagli, M. Cantarero, Cucci L., D'Amico S., De Beni E., De Martini P. M., Mariucci  
 974 M. T., Messina A., Montone P., Nappi R., Nave R., Pantosti D., Ricci T., Sapia V., Smedile A.,  
 975 Vallone R. & Venuti A., 2020. Surface ruptures database related to the 26 December 2018, MW  
 976 4.9 Mt. Etna earthquake, southern Italy. *Scientific data*, 7(1), 1–9.

977 Vollgger, S.A., Cruden, A.R. (2016). Mapping folds and fractures in basement and cover rocks using  
 978 UAV photogrammetry, Cape Liptrap and Cape Paterson, Victoria, Australia. *J. Struct. Geol.*, 85,  
 979 168–187.

Formattato: Inglese americano

Formattato: Inglese americano

Formattato: Italiano

Formattato: Non regolare lo spazio tra testo asiatico e in alfabeto latino, Non regolare lo spazio tra testo asiatico e caratteri numerici

Formattato: Inglese (Regno Unito)

Formattato: Tipo di carattere: Non Corsivo, Inglese americano

Formattato: Tipo di carattere: (Predefinito) Verdana, 10 pt

Formattato: Inglese (Regno Unito)

Formattato: Tipo di carattere: Non Corsivo, Inglese (Regno Unito)

980 Walter, T.R., Acocella, V., Neri, M., Amelung, F. (2005). Feedback processes between magmatism  
981 and E-flank movement at Mt. Etna (Italy) during the 2002-2003 eruption. J. Geophys. Res., 110,  
982 B10205, doi:10.1029/2005JB003688.

983 [Weismüller, C., Urai, J.L., Kettermann, M., Hagke, C.V., Reicherter, K. \(2019\). Structure of massively](#)  
984 [dilatant faults in Iceland: lessons learned from high-resolution unmanned aerial vehicle](#)  
985 [data. Solid Earth, 10\(5\), 1757-1784.](#)

986 Westoby, M.J., Brasington, J., Glasser, N.F., Hambrey, M.J., Reynolds, J.M. (2012). 'Structure-from-  
987 Motion' photogrammetry: a low-cost, effective tool for geoscience applications.  
988 Geomorphology, 179, 300–314.

989

Formattato: Inglese (Regno Unito)

Formattato: Tipo di carattere: Non Corsivo, Inglese (Regno Unito)

Formattato: Inglese (Regno Unito)

Formattato: Tipo di carattere: Non Corsivo, Inglese (Regno Unito)

Formattato: Inglese (Regno Unito)